ELECTRON TECHNOLOGY
ISSN 1897-2381
http://www.ite.waw.pl/etij/
Internet Journal

HAADF-STEM IMAGING AND MICROSCOPY OBSERVATIONS OF HETEROSTRUCTURES IN ELECTRONIC DEVICES

J. M. SHIOJIRI*

Kanazawa Medical University, Ishikawa 920-0293, Japan
Kyoto Institute of Technology, Kyoto 606-8585, Japan

Received February 7, 2004; published April 2, 2004

ABSTRACT

Atomic resolved high-angle annular dark field (HAADF) scanning transmission electron microscopy (STEM), which has been widely used for the analysis of crystal and defect structures, is a quite new technique developed in this decade and its imaging mechanism is quite complicated. The first part of this paper is devoted to physics to understand HAADF-STEM imaging. Then, our recent investigations of GaN-based laser diodes are reviewed which were performed by HAADF-TEM and high-resolution field-emission scanning electron microscopy.

1. Introduction

Devices such as quantum wells lasers, tunneling devices, access memory devices and high electron mobility transistors comprise multiplayer hetero-structures, which are produced by atomic-scale controlling. Therefore, atomic-scale structural and chemical analysis is demanded for the understanding and improvement of physical or functional properties and the quality control of the products. High-resolution transmission electron microscopy (HRTEM) is a powerful tool for this demand, and has been successfully employed for characterization of many devices. Selected area electron diffraction, energy dispersive X-ray spectroscopy (EDXS), and electron energy-loss spectroscopy (EELS) provide complementary information.

We investigated InGaAs/InP crystals with the (001)-multilayer heterostructure grown by the metalorganic vapor phase epitaxy method, by HRTEM with the aid of image simulation [1, 2]. It was found that atoms do not diffuse near the interfaces of InP → InGaAs following growth direction but do diffuse near the interfaces of InGaAs → InP. The formation of defects in III-V heterostructures was investigated by conventional (C-) TEM and HRTEM, in the cooperation with the Institute of Electron Technology (IET) in Warsaw [3]. GaAs/$Al_{0.4}Ga_{0.6}As$ heterostructures were grown by the liquid phase epitaxy method at IET [4, 5]. Using a skilful image processing we identified regularly shaped crystallites as FeAs with a definite orientation with respect to the GaAs crystal. EDXS analysis confirmed this result. The contamination of the heterostructure surface by Fe atoms, followed by their migration from the surface during annealing, can be responsible for the formation of the FeAs precipitates [6]. A multilayer heterostructure of AlAs (2 nm)/GaAs(4 nm)/AlGaAs(3 nm) between the GaAs substrate and the GaAs capping layer, was prepared by molecular beam epitaxy. In spite of damages caused during ion milling in specimen preparation for electron microscopy, Ga and As atom columns in the GaAs layer and Al and As atom columns in the AlAs layer were identified in the (110) HRTEM images, with the aid of image simulation and processing [7]. The average and the variance of the widths of the AlAs, GaAs, and AlGaAs layers were estimated from the small-angle scattering image reconstructed from the HRTEM image.

Advance field-emission electron microscopes allow the EDXS and EELS elemental mapping of specimens. Kawasaki et al. [8, 9] reported the elemental distribution in an O-N-O dielectric multi-layer within the dynamic random access memory (DRAM) device. The nominal structure of the insulator O-N-O layer is SiO_2 (2.2 nm)/Si_3N_4 (5.7 nm)/ /SiO_2 (2.6 nm) between the single-crystal Si substrate and the P-doped poly-crystalline Si layer in the

*Honorary member of the Polish Society for Microscopy. Home address: 1-297 Wakiyama, Enmyoji, Kyoto 618-0091, Japan. e-mail: shiojiri@pc4.so-net.ne.jp

capacitor region. The distribution of Si, P, O, and N atoms was visualized in EDXS mapping [8] and EELS mapping [9].

High-angle annular dark field (HAADF) scanning transmission microscopy (STEM) is a quite new technique developed in this decade, and has been used to analyze lattice defects as well as crystal structures [10]. The HAADF-STEM image is called *Z*-contrast image because of strong contrast dependence on the atomic number. Its imaging is completely different from CTEM and HRTEM and is quite complicated. The first part of this paper is devoted to physics to understand HAADF-STEM imaging, showing our investigations concerning the basis of HAADF-STEM. Then, our HAADF-STEM investigations on multiplayer heterostructures in the GaN-based laser-diode are reviewed. High-resolution field-emission scanning microscopy (FE-SEM) observations of these heterostructures are also reproduced.

The present paper would be devoted to Prof. Julian Auleytner, Institute of Physics, Polish Academy of Sciences (PAS), Warsaw, who passed away on December 7, 2003. Our successive and successful scientific collaboration with Polish scientists, which have been made since 1985, would not present without Prof. Auleytner, particularly, the joint project between IET and Kyoto Institute of Technology or Toyama University from 1995 until 2003 which was authorized by the Polish and Japanese Governments. In September 1997, the 1st Polish-Japanese Joint Seminar on Materials Analysis was held as one of activities of this Project. The 5th Joint Seminar shall be held in August 2004.

2. HAADF-STEM

First, we confirm the terms of 'coherence' and 'incoherence' [12]. It is a fundamental concept of quantum mechanism that a quantum particle also behaves as a wave. As well known, the waves passed through different holes interfere with each other to show Young's fringes. The interference also occurs between the electron waves scattered by different atoms. But it can take place only between elastically scattered electron waves or between inelastically scattered electron waves with the same wavelength. The former gives Bragg reflections. Hereafter we call the scattering that causes Bragg reflections 'Bragg scattering'. The 'elastic scattering' is no energy-loss scattering. According to quantum mechanism, the interference never occurs between waves of different electrons [13]. Thus, the interference takes place only between the waves with the same wavelength incorporated with 'a single electron'. The electron is observed in terms of the intensity I, which gives a probability of the appearance. The position of the detected electron does not show its real place but indicates only a place where it was accidentally captured. For the visualization of the whole probable position of electron we need the detection of many electrons that are captured at a region assigned with the same interference condition [14]. The waves of these electrons are 'coherent' with each other, and show a physically valuable intensity distribution (such as interference fringes or diffraction spots) as a result of the cooperation. Thus, 'interference' is a term for showing the intra-electron relation of waves, while the term of 'coherence' or 'incoherence' should be used for showing the inter-electron relation between the waves that belong to different electrons. In other words, the interference is described as $\Phi_j = \Sigma_i \phi_{ij}$, where ϕ_{ij} is the wave of an electron j elastically scattered by the atom i, while the coherence and incoherence are described as $I = \Sigma_j I_j = \Sigma_j |\Phi_j|^2$, where $I_j = |\Phi_j|^2$ is the interference intensity for the electron j. The coherence is in the case of that all Φ_j are the same, that is, $I = n|\Phi|^2$ where n is the number of electrons. Thus, only the waves for electrons which have the same birth place (the source and scattered positions) and the same energy are coherent. A field-emission gun can supply a coherent electron beam because it provides the same source at the top of the tip and gives the same energy to the emitting electrons. We can use the term of 'partial coherence' when the source position and/or energy of electrons are the same only within a permissible limit given by the Rayleigh criterion, that is when the spatial coherence and/or the time coherence are not completely but partially satisfied to recognize the interference fringes.

All atoms in the specimen vibrate thermally around their equilibrium positions. The waves of electrons elastically scattered at the equilibrium positions are completely coherent with each other, and therefore give rise to Bragg reflections. The atoms differently displaced from the equilibrium positions also do elastically scatter electrons. The waves of these electrons are incoherent with each other because of spatial difference of the resources. The frequency of the thermal lattice vibration ~ 10^{13} Hz is the fifth power of 10 times as small as a frequency of incident electron wave ~10^{18} Hz, so that the displacements are observable using the electron beam. The scattering from the displaced atoms, thus, gives diffuse intensity distribution. This is 'thermal diffuse scattering' (TDS). We assume Einstein model where the atoms moving independently with each other. By taking the mean squared displacement, the Debye-Waller factor was led [15]. Frozen phonon method is another approach, where thermal vibration of atoms is simulated on a computer and then the intensities of Bragg scattering and TDS are numerically deduced by summing up those intensities at several moments [16]. However, the incident electrons may be considered to interact

inelastically with phonons, which are quantized particles representing the lattice vibration, losing or gaining energy ΔE, during the collision. The energy of phonons is in the order of 10^{-1} eV or less (~infrared radiation) and that of the incident electrons is 10^{5} eV so that ΔE is negligibly small. Hence, the TDS can be treated as elastic, incoherent scattering, while Bragg scattering is elastic, coherent scattering. Thus, their intensities are given by the formulae shown in Fig. 1.

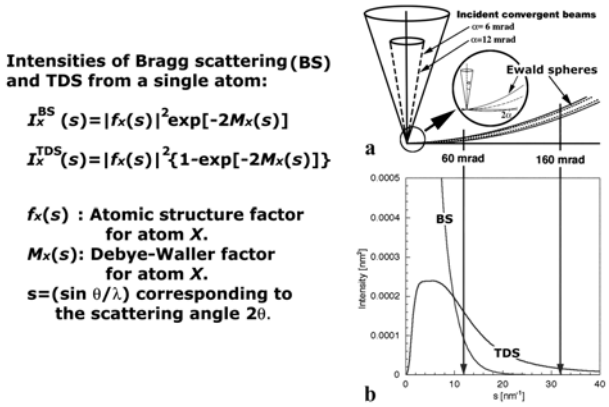

Fig. 1. Intensity of Bragg scattering (BS) and thermal diffuse scattering (TDS) for a single atom. a) Schematic Ewald sphere construction of HAADF-STEM, indicating the relation between the incident convergent beam and the annular detector. The case for the beam probe with semi-angle α = 6 or 12 mrad and the collecting range of the detector D = 60 ~160 mrad is indicated. b) Intensity of BS and TDS from a single Si atom as a function of scattering angle. The integration of the intensity over the collecting range gives the cross section or the detection intensity, and then TDS is the principle part in HAADF-STEM imaging.

The electron beam runs in reverse between the STEM and CTEM (Fig. 2). A STEM image is a focal signal recorded on the detector as a function of the probe position. Bright field (BF) STEM imaging is explained to be equivalent to CTEM imaging in terms of the reciprocity rule (strictly in case of use of an ideal point detector) [17], and then is greatly influenced by the imaging condition; defocus, thickness and so on [10]. The high-angle annual detector is used to exclude Bragg scattering and eliminate this phase problem [18], so that the contrast of HAADF-STEM images never reverses by the change of defocus and thickness. As seen in Fig. 1a, all the reciprocal points within a scattering angle of 2α in the zero-order Laue zone (ZOLZ), where α is the semi-angle of probe, are placed on one of Ewald spheres so that Bragg reflections take place. In a high angle range, the reciprocal points not only in ZOLZ but also in low higher-order Laue zone (HOLZ) do not cross with any Ewald sphere. Furthermore, the intensity of the Bragg scattering reduces greatly with increasing scattering angle as shown in Fig. 1b, comparing with TDS intensity. Therefore, Bragg reflections scarcely influence HAADF-STEM imaging. TDS is an origin of unfavorable background, particularly in a high angle range, in electron diffraction and X-ray diffraction, but it plays the principal part in HAADF-STEM imaging.

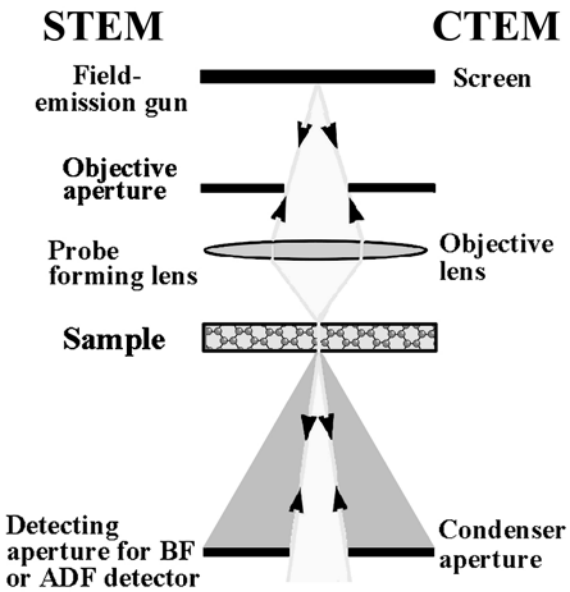

Fig. 2. Ray diagram of scanning transmission electron microscope (STEM) and conventional transmission electron microscope (CTEM). The ray runs downward in STEM and upwards in CTEM. According to the reciprocity rule of optics, bright field STEM and CTEM give rise to the same image contrast due to elastic, coherent scattering (Bragg scattering). HAADF-STEM imaging, mainly due to elastic, incoherent scattering (TDS) is completely different from CTEM imaging.

In atomically resolved HAADF-STEM, the contrast of an atomic column is obtained as the integrated intensity for exposure, since the atoms in the column are different in position at different moments so that scatter electrons incoherently as TDS. This is one of the reasons why HAADF-STEM image is incoherent, and may be called 'laterally incoherent'. Another reason of the incoherent imaging is ascribed to scanning of the convergent beam. The electrons scattered from an atomic column might be different from those scattered from different atomic columns because time is different. Therefore the columns separated laterally are imaged incoherently, that is, a STEM image is transversally incoherent by nature. Therefore, HAADF-STEM imaging is incoherent [12].

On the base of this principle, one can write STEM image simulation programs. We have developed a program for BF and ADF-STEM simulations [19]. The algorithm is based on Bethe method using two kinds of optical potentials [20], and contains calculation programs for the Bragg scattering and TDS. Our scheme reduces drastically the computing time as illustrated in the reference 12, and allows routine works of ADF-STEM image simulation, accordingly.

We examined systematically the influence of the optical parameters; the spherical aberration of the probe-forming lens C_s, the defocus Δf, the semi-angle of the probe α [21, 22] and the collection angle range of the annular detector D [23], on the HAADF-STEM images. The artifacts are typical of the influence and may mislead the structure analysis unless one finds them from image simulation [24]. Paradoxically speaking, the simulation of HAADF-STEM images provides the structural and compositional information of every atomic column along the incident beam. In fact, we have reported HAADF-STEM concentration analyses of As atoms along every [110] column in As-doped Si wafers (Fig. 3) [25] and Bi atoms along every [001] column in the boundary layer in $Sr(Bi)TiO_3$ ceramic condensers, with the aid of the image simulation [26].

The contrast of the HAADF-STEM image is given by the sum of the intensity of TDS electrons collected on the detector. Each atom ejects TDS electrons depending on the wave field of the incident electrons in the crystal. The cross section for TDS is different among atom species. Therefore, the intensity in HAADF-STEM images depends on the atomic number and the number of atoms along atomic columns in the specimen. Thereby, we determined the film thickness of $SrTiO_3$ from HAADF-STEM image simulation [27]. The image contrast dependence on thickness was experimentally examined in HAADF-STEM images of [011] Si [23] and $CaTiO_3$ [22], and in MAADF-STEM images of Si [23]. The wave field in the crystal is influenced by lattice distortion, which is caused by substituted impurity atoms, or a small tilt of the zone-axis with respect to the incident beam direction. The effect of the lattice distortion on the HAADF-STEM images was examined using $SrTiO_3$ [26, 27] and that of the small crystal tilt using the [011] Si [28].

However, if a HAADF-STEM image is influenced only by the probe, the Z-contrast image or the projected atomic structure may be obtained by image processing which removes the effect of the probe from the image. We have shown that the deconvolution processing retrieves unfavorable experimental images. Images having the artificial bright spots or unresolved Si dumbbells approximated to the projected atomic structure [29]. The process has been extended for HAADF-STEM images, which are often systematically distorted by environmental and/or instrumental instability in today's field-emission electron microscopes [30]. Thus, we have two approaches to the structural and chemical analysis by HAADF-STEM; the image simulation and the retrieval image processing. These two approaches have been discussed, illustrating images of Sb-rich inversion boundaries in ZnO ceramics [31].

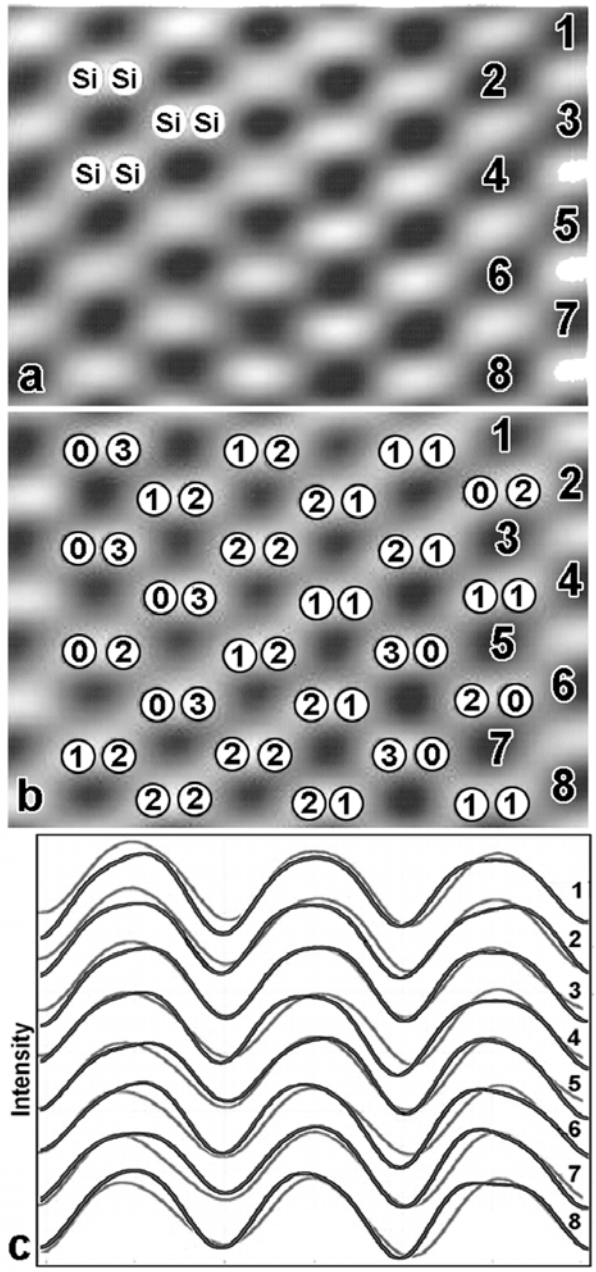

Fig. 3. a) Experimental (noise-filtered) HAADF-STEM image of [110] Si wafer implanted with 0.5 at. % As. The Si dumbbells are not resolved under this imaging condition [21], [24]. b) Experimental (noise-filtered) HAADF-STEM image of a [110] Si wafer implanted with 1.9 at. % As. Insets are evaluated number of As atoms substituted for Si atoms in 65 atom sites along each [110] column in the crystal 25 nm thick. The thickness was determined from the image simulation. c) Intensity profiles along rows 1-8 in (a and b). Most of the Si dumbbells in (a) are symmetric (see fine curves), which means the atom sites are occupied only by Si, while ones in (b) are asymmetric due to the substitution of As atoms (see thick curves). The number of As atoms in (b) were determined from the simulation of the intensity profiles [25]. (The image was taken by Dr. M. Kawasaki, JEOL US, with a JEM 2010-TEM/STEM (C_s = 1.0 mm) operated at V = 200 keV. The defocus Δf = –50 nm, the semi-angle of the probe α = 6 mrad, and the collecting range of the annular detector D = 50 ~ 110 mrad).

3. Structure analysis of GaN-based laser diodes by HAADF-STEM and FE-SEM

GaN has a wide band gap of 3.4 eV and therefore has provided its attractive application for electronic devices, such as light-emitting diodes and violet or purple emitting lasers [32, 33]. The lifetime of a violet laser diodes (LDs) with multiple quantum wells (MQW) InGaN/GaN and separate-confinement heterostructure (SCH) AlGaN/GaN has attained to more than 10,000 h [34]. This was achieved by the epitaxially lateral overgrowth of GaN layer on the sapphire substrate [35, 36] and the cladding of AlGaN/GaN strained-layer superlattices (SLSs) [34]. The former causes the reduction of dislocation density. The latter is used for the following two reasons. Thick AlGaN cladding layers need for optical confinement, but cracks and dislocations induced by the lattice mismatch between GaN and AlGaN make the formation of the thick cladding layers impossible. It is the first reason to depress the formation of these defects by strain relief of the AlGaN/GaN SLSs [33]. The second one is that Mg-doped AlGaN/GaN SLSs have also an enhanced hole concentration over $3 \cdot 10^{18}$ cm^{-3} at room temperature, which is more than ten times that obtained in bulk AlGaN layers [37, 38].

Tu et al. [39, 40] have developed MQW InGaN/GaN / SCH GaN/AlGaN violet LDs including Si-doped *n*-type and Mg-doped *p*-type SLS $Al_{0.14}Ga_{0.86}N$/GaN cladding layers, as schematically shown in Fig. 4. The LDs were directly grown on a (0001)-face sapphire substrate by production-scale metalorganic vapor phase epitaxy system. The threshold current density of the LDs was 8.7 kA/cm^2, and the strong simulated emission was observed at around 415.5 nm with two small emission peaks of 416 nm and 417 nm. In the present microscopy observations prototypes of this LD where some parts of the LD were not deposited were used.

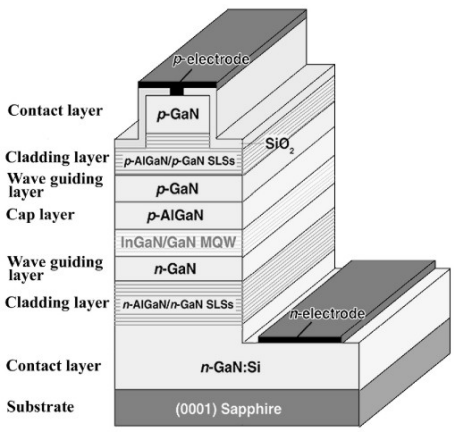

Fig. 4. Schematic structure of the ridge-waveguide InGaN/GaN laser with $Al_{0.14}Ga_{0.86}N$/GaN strained-layer superlattice (SLSs) cladding layer, prepared by production-scale metalorganic vapor phase epitaxy system in the Opto-Electronics and Systems Laboratories, Industrial Technology Research Institute, Taiwan [39].

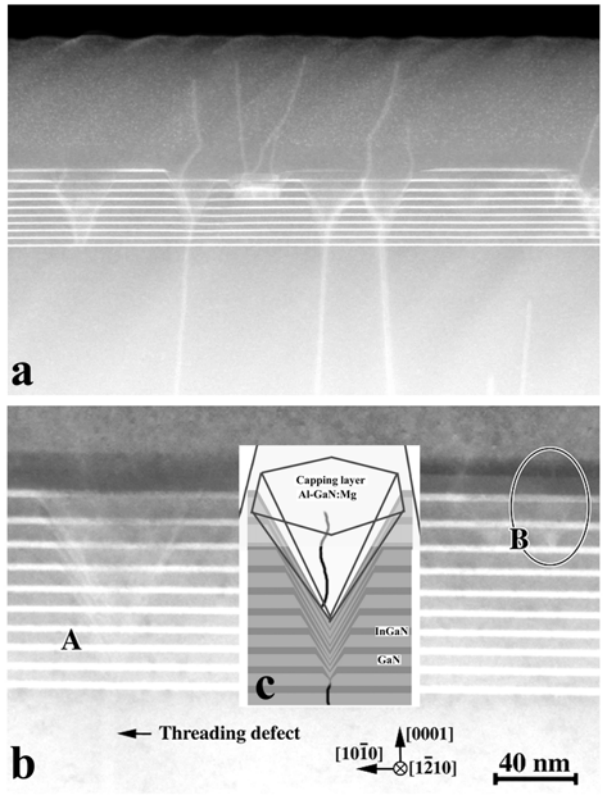

Fig. 5. a) Cross-sectional low magnified HAADF-STEM image of capped MQW InGaN/GaN. Ten bright stripes parallel to the basal plane are InGaN layers. Threading defects, which were formed by large lattice mismatch between the GaN and sapphire are observed as bright lines along the [0001] direction. *V*-defects nucleate at the threading defects in the MQWs layers. b) Enlarged HAADF-STEM image of another part. *V*-defect **A** reveals that it grew in the form of a thin six-walled structure with InGaN/GaN {101} layers as illustrated in (c). These thin MQWs layers may be responsible to additional small peaks around the strong simulated laser emission. V-defect **B** nucleated at a large bright spots, which were the In rich region in the InGaN layer. c) Schematic representation of *V*-defect, which is an open hexagonal inverted pyramid with the sidewall quantum wells on the {101} planes and filled with capping matrix afterward. The apex is at the terminal of a threading defect in the InGaN layer [45]. (The images were taken by Mr. K. Inoke, FEI, with a Tecnai F30 (C_s = 1.2 mm) operated at V = 300 keV. The imaging condition: Δf = –49 nm, α = 26 mrad, D = 36 ~ 190 mrad).

We performed HAADF-STEM observations of the MQW InGaN/GaN layers. Even low magnification HAADF-STEM images gave certain information about the structure and composition of the ultrathin InGaN layer. Figure 5a shows the low magnified image. Bright bands are $In^{49}Ga^{31}N^7$ layers and dark ones are $Ga^{31}N^7$ layers. This was confirmed by EDXS [41]. Threading defects, which were formed from the big lattice misfit between the GaN and sapphire, are seen with bright contrast due to large distortion around the defects. High-resolution HAADF-STEM image, processed by the deconvolution method [29], clearly defined the interface between InGaN and GaN layers at the

atomic scale [41], as seen in Fig. 6a. HAADF-STEM also revealed *V*-defects or inverted hexagonal pyramid defects (IHPs) (Fig. 5a and **A** in Fig. 5b). The names come from the empty *V*-pit in hexahedron cone sharp, with six sidewalls on {101} planes, which nucleates at a threading dislocation or nano-pipes extending along the [0001]-axis growth direction, in the InGaN layers [42–44]. Figure 5b shows that the *V*-defects grew in the form of a thin six-walled structure with InGaN/GaN {101} layers as schematically shown in Fig. 5c [45], although Sharma et al. [46] reported the InGaN MQWs ending abruptly at the *V*-defect interfaces. We also found that the *V*-defects start even at In-rich dots under adverse growth conditions, as B in Fig. 5b did so [45]. The side-walled InGaN/GaN layers might cause unfavorable weak long-wavelength emissions similarly as different-thickness MQWs do, like the 416-nm and 417-nm emissions in the 415-nm LD. The detection and control of these *V*-defects are, therefore, very important for fabrication of these LDs.

The HAADF-STEM image (Fig. 6a), processed by two-dimensional smoothing and deconvolution, provides precise positions of the atomic columns (Fig. 6b) and clear atomic number dependent

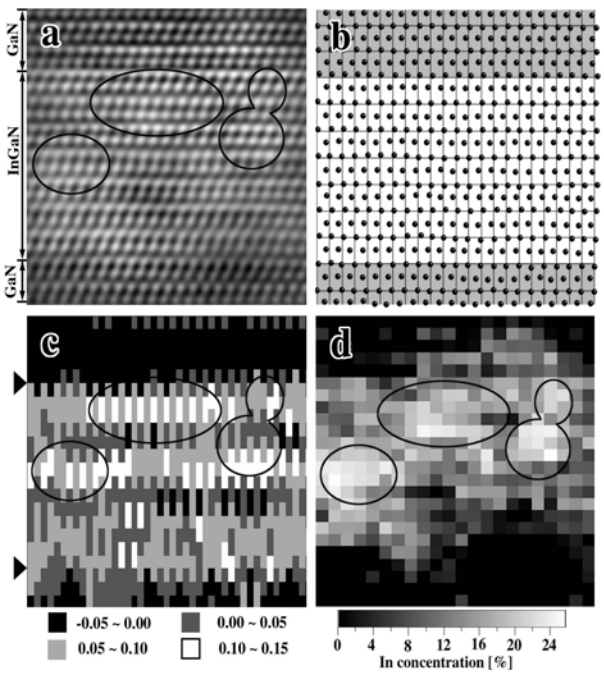

Fig. 6 a) Experimental deconvolution-processed [29] high-resolution HAADF-STEM image of the MQWs InGaN/GaN layers, taken with Tecnai F30. The defocus of the probe-forming lens was evaluated to be $\Delta f = -44$ nm in deconvolution process. b) Projected atomic column positions derived from (a). The distortion hardly occurred along the [100] direction. c) Strain field maps along the [0001] direction. Arrowheads show the interfaces between GaN and InGaN layers. d) Two-dimensional In atom distribution. There is local fluctuation of In atoms in the InGaN layers, and the In-rich regions enclosed, considered as quantum dots, cause large expansion only along the [0001] direction.

contrast, thereby allowing us to map both the strain field (Fig. 6c) and In atom distributions (Fig. 6d) in successive GaN and InGaN layers [47]. The lattice expands largely along the [0001] direction as seen in Fig. 6c but hardly along the $[1\bar{1}00]$ direction in the InGaN layers [47]. These maps indicated local fluctuations of In atoms in the InGaN layers and revealed that the In-rich regions, considered to be quantum dots, cause lattice expansion only along the [0001] direction.

Recently, we have succeeded in distinguishing the MQW $In_{0.25}Ga_{0.75}N$ (2.5 nm) and GaN (13.9 nm) layers in a secondary electron image and a back-scattered electron image in a high-resolution field-emission scanning electron microscope (FE-SEM), and confirmed the formation of the thin six-walled structure of the *V*-defect [48]. The observed images resemble to the HAADF-STEM images in Fig. 5. The secondary electron mode shows the topographic contrast of the specimen surface while the back scatttered electron mode, when a YAG detector is used, provides rather the composition information. The advantage of the SEM observations is in the very simple specimen preparation. There is no risk of structural, compositional and energetic changes due to damage and/or contamination during thinning treatments, which are necessary for TEM and STEM. The images do not suffer from topological effects such as lattice distortion and free from creation of artifacts.

With regard to the AlGaN/GaN SLS cladding layers, there are very few reports on the structural analysis although their structure greatly influences the laser properties. Bremser et al. [49] and Pecz et al. [50] observed AlGaN/GaN layers by CTEM. The diffraction contrast due to small strain field along the interfaces between AlGaN and GaN layers indicated these thin layers distinguishably. However, the observed fringes did not show the real widths of AlGaN and GaN layers. HRTEM observation could not identify $Al_{0.14}Ga_{0.86}N$ layers and GaN layers in the cladding (Fig. 7a), which was confirmed by image simulation [51]. We have been observing the SLSs, which are 200 coupled layers of *n*-$Al_{0.14}Ga_{0.86}N$(3 nm)/*n*-GaN (3 nm) on the *n*-GaN:Si grown directly on a (0001) sapphire substrate. The $Al^{13}Ga^{31}N^{7}$ and $Ga^{31}N^{7}$ layers exhibit dark and bright fringes, respectively, in the $[10\bar{1}0]$ HAADF-STEM image (Fig. 7b) [52]. With the aid of image processing, the averaged thickness of the AlGaN and GaN layers was determined to be 2.24±0.09 nm and 2.34±0.15 nm, respectively, which correspond to nine atomic layers in the [0001] direction of GaN. We also observed some extended defects, running either parallel or perpendicular to the GaN [0001] axis (Fig. 7c) [52]. These defects along the [0001] axis might be the threading defects. When they reach the MQW InGaN/GaN layers, they create *V*-defects, which are quite unfavorable to the laser emission, as

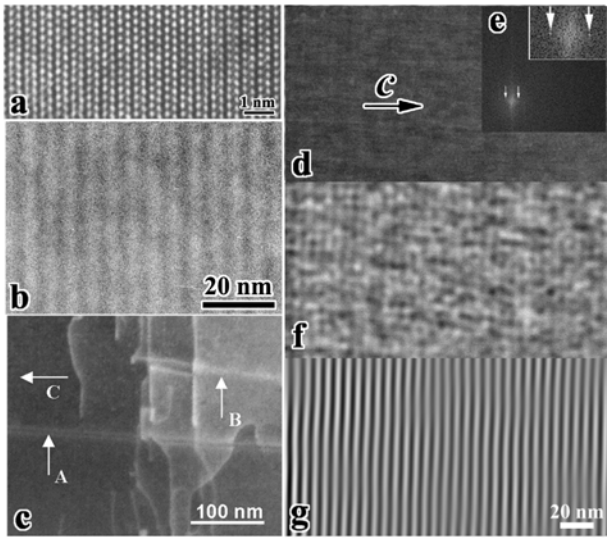

Fig. 7 a) Experimental HRTEM image of SLSs *n*-$Al_{0.14}Ga_{0.86}N$ (3 nm)/*n*-GaN(3 nm) layers that grew on the *n*-GaN:Si deposited on a (0001) sapphire substrate. The AlGaN and GaN layers cannot be distinguished in the HRTEM image. b) Experimental HAADF-STEM image of the same specimen, distinguishing between the AlGaN(dark stripes) and GaN layers (bright stripes). c) Low magnified experimental HAADF-STEM image. Threading defects **A** and **B** run along *c*-axis, exhibiting bright contrast due to lattice distortion (or precipitated impurities). Note defect **B** turning its course from running along the *c*-axis to lying in the basal plane. It apparently cannot reach the MQW. As a result the number of defects in MQW is reduced. d) Experimental second electron image of the same sample. e) Computed diffractogram of the image (a) with its enlarged central part. f) Noise-filtered image taken from the diffractogram (e). g) Image reconstructed using only diffraction spots indicated by arrowheads in (e). The contrast of superlattices was enhanced and surface structure suppressed. (The image in (a) was taken by Dr. S. Strum, J. Stefan Institute, with a JEM-2010F TEM/STEM (C_s = 0.48 mm) operated at V = 200 keV. The images in (b) and (c) were taken by Dr. M. Čeh, with the same microscope. Imaging condition: Δf = the optimum condition, α = 10 mrad, D = = 100~220 mrad. The image in (d) was taken by Ms. M. Nakagawa, Hitachi Science Systems, with a Hitachi S-5200 UHR FE-SEM. Imaging condition: V = 10.0 keV. The imaging processing was performed by Dr. A. Rečnik).

described above. The bright lines parallel to the basal planes seem to originate from these threading defects. They revert from running along the [0001] axis to lying in the basal plane and apparently cannot reach the MQW. As a result the number of defects in MQW is reduced. This evidently shows the suppressing role of SLSs in the defect propagation, which results in the overall reduction of the structural defects in the active MQW layer.

The same SLS sample was observed in the FE-SEM [51]. Figure 7d shows the original secondary electron image taken at 10.0 keV, and its computed difffractogram is indicated in Fig. 7e. Figure 7f is the reconstructed image from the diffractogram by filtering high and low spatial frequency noises. Fringes parallel to the basal plane are seen together with a fine surface structure (nearly parallel to the [0001] axis) formed by cleaving. The fringes are ascribed to the SLSs, because of a spacing of ~3 nm that corresponds to the thickness of the $Al_{0.14}Ga_{0.86}N$ and GaN layers. Figure 7g is a processed image which was reconstructed using only the diffraction spots indicated by arrowheads in Fig. 7e and enhanced the SLSs. The fringes due to SLSs were also observed in the secondary electron images taken at different voltages such as 25 keV, but they could not be detected in the back scattered electron images from the primary electrons at 10~25 keV. This is obvious because the mass difference between $Al_{0.14}Ga_{0.86}N$ and GaN is small, and the image contrast in the back scattered or Rutherford electrons is undetectable. The secondary emission yield is greatly depending on the surface state of materials so that we might resolve the $Al_{0.14}Ga_{0.86}N$ and GaN layers in the secondary electron images. We also observed the *p*-$Al_{0.14}Ga_{0.86}N$(3.0 nm)/*p*-GaN(3.0 nm) structure at the same imaging conditions. No contrast fringes were detected neither in the secondary electron image nor in the back scattered one. Difference in the secondary emission yields between *p*-$Al_{0.14}Ga_{0.86}N$ and *p*-GaN seems to be very small.

In conclusion, HAAD-STEM would become very powerful tool for characterization of nano-devices having atomic-scale heterostructure because it allows atomic-scale chemical analysis. Advanced high-resolution SEM is also applicable to characterization of these devices.

Acknowledgements

Deep thanks are owing to collaborators, without whom the investigations have never been achieved. Their names are on our papers in references. Thanks to collaboration with Prof. J. Kątcki, IET, Prof. I. M. Sosnowska and Dr. R. Przeniosło, Warsaw University, Prof. J. Dutkiewicz, Institute of Metallurgy and Materials Science, PAS, Prof. A. Czyrska-Filemonowicz, University of Mining and Metallurgy, Prof. H. Meczynska and Dr. F. Firszt, N. Copernicus University, Drs. P. Dluzewski and W. Paszkowicz, Institute of Physics, PAS, Prof. M. Suszyńska, Institute of Low Temperature and Structure Research, PAS, and Prof. A. Zaleski, Wrocław University of Technology. I had an idea to write this paper devoted to Prof. J. Auleytner. Thanks are also to Mr. M. Asanuma, JEOL Europe and Ms E. Kobayashi, worked at FEI Japan, for encouraging help for this work.

References

1. Y. Yabuuchi, Y. Takahashi, N. Ohtsuka, T. Isshiki, M. Tujikura, H. Saijo, M. Shiojiri, phys. stat. sol. (a) 1991, **127**, 385.

2. M. SHIOJIRI, T. ISSHIKI, K. NISHIO, M. TSUJIKURA, H. SAIJO, Y. TAKAHASHI, N. OHTSUKA, Y. YABUUCHI, J. Electron Microscopy, 1992, **41**, 438.
3. J. KĄTCKI, J. RATAJCZAK, F. PHILLIPP, N.Y. JIN-PHILLIPP, M. SHIOJIRI, Proc. of the Int. Symp. on Hybrid Analyses for Functional Nanostructure, Kyoto, 1998, 133.
4. J. KĄTCKI, M. SHIOJIRI, T. ISSHIKI, K. NISHIO, Y. YABUUCHI, N.Y. JIN-PHILLIPP, Electron Technol. 1996, **29**, 393.
5. J. KĄTCKI, M. SHIOJIRI, T. ISSHIKI, K. NISHIO, Y. YABUUCHI, N.Y. JIN-PHILLIPP, Inst. Phys. Conf. Ser. No. 157, *Microscopy of Semiconducting Materials*, 1997, IOP Publ., Bristol, 295–298.
6. J. KĄTCKI, M. SHIOJIRI, T. ISSHIKI, K. NISHIO, Y. YABUUCHI, N. Y. JIN-PHILLIPP, J. Electron Microscopy, 1998, **47**, 575.
7. K. NISHIO, J. KĄTCKI, M. SHIOJIRI, Electron Technol., 1999, **32**, 348.
8. M. KAWASAKI, T. OIKAWA, K. IBE, K. PARK, M. SHIOJIRI, J. Electron Microscopy, 1998, **47**, 335.
9. M. KAWASAKI, T. OIKAWA, K. IBE, K.H. PARK, M. SHIOJIRI, J. Electron Microscopy, 1998, **47**, 477.
10. S. J. PENNYCOOK, P. D. NELLIST P D, in *Impact of Electron and Scanning Probe Microscopy on Materials Research*, D. G. Rickerby, G. Valdre and U. Valdre (Eds.), Kluwer Academic Publ., Dordrecht, 1999, 161–207.
11. M. SHIOJIRI, in: *Defects in Crystals*, E. Mizera (Ed.), World Sci., Singapore, 1987, 291–303.
12. M. SHIOJIRI, T. YAMAZAKI, JEOL News, 2003, **38**, 54.
13. P.A.M DIRAC, *The Principles of Quantum Mechanics*, 3rd Ed., Oxford University Press, London, 1947.
14. A. TONOMURA, *The Quantum World Unveiled by Electron Waves*, World Sci., Singapore, 1998.
15. R. W. JAMES, *The Optical Principles of The Diffraction of X-RAys*, G. Bell a. Sons, London, 1948.
16. R. F. LOANE, P. XU, J. SILCOX, Acta Crystallogr., 1991, **A47,** 267.
17. J. M. COWLEY, Appl. Phys. Lett., 1969, **15,** 58.
18. A. HOWIE, J. Microscopy, 1979, **117,** 11.
19. K. WATANABE, T. YAMAZAKI, HASHIMOTO, M. SHIOJIRI, Phys. Rev. B, 2001, **64,** 115432.
20. P. B. HIRSCH, Proc. Roy. Soc. of London A 1965, **286,** 158.
21. K. WATANABE, N. NAKANISHI, T. YAMAZAKI, M. KAWASAKI, I. HASHIMOTO and M. SHIOJIRI, phys. stat. sol. (b) 2003, **235,** 179.
22. S. ŠTURM, A. REČNIK, M. KAWASAKI, T. YAMAZAKI, K. WATANABE, M. SHIOJIRI, M. ČEH, JEOL News, 2002, **37E**, 22.
23. K. WATANABE, T. YAMAZAKI, I. HASHIMOTO, M. SHIOJIRI, Phys. Rev. B, 2001, **64,** 115432.
24. K. WATANABE, T. YAMAZAKI, Y. KIKUCHI, Y. KOTAKA, M. KAWASAKI, I. HASHIMOTO, M. SHIOJIRI, Phys. Rev. B, 2001, **63,** 085316.
25. T. YAMAZAKI, K. WATANABE, Y. KIKUCHI, M. KAWASAKI, I. HASHIMOTO, M. SHIOJIRI, Phys. Rev. B, 2000, **61,** 13833.
26. M. KAWASAKI, T. YAMAZAKI, S. SATO, K. WATANABE, M. SHIOJIRI, Philos. Mag. A, 2001, **81,** 245.
27. T. YAMAZAKI, K. WATANABE, A. REČNIK, M. ČEH, M. KAWASAKI, M. SHIOJIRI, J. Electron Microscopy, 2000, **49,** 753.
28. T. YAMAZAKI, M. KAWASAKI, K. WATANABE, I. HASHIMOTO, M. SHIOJIRI, Ultramicroscopy, 2002, **92,** 181.
29. K. WATANABE, Y. KOTAKA, N. NAKANISHI, T. YAMAZAKI, I. HASHIMOTO, M. SHIOJIRI, Ultramicroscopy, 2002, **92**, 191.
30. N. NAKANISHI, T. YAMAZAKI, A. REČNIK, M. ČEH, M. KAWASAKI, K. WATANABE, M. SHIOJIRI, J. Electron Microscopy, 2002, **51,** 383.
31. T. YAMAZAKI, N. NAKANISHI, A. REČNIK, M. KAWASAKI, K. WATANABE, M. ČEH, M. SHIOJIRI, Ultramicroscopy, 2004, **98**, 305.
32. H. AMANO, N. SAWAKI, I. AKASAKI, Y. TOYODA, Appl. Phys. Lett., 1986, **48**, 353, 353.
33. S. NAKAMURA, M. SENOH, S. NAGAHAMA, N. IWASA, T. YAMADA, T. MATSUSHITA, H. KIYOKU, Y. SUGIMOTO, Jpn. J. Appl. Phys., 1996, **35**, L74.
34. S. NAKAMURA, M. SENOH, S. NAGAHARA, N. IWASA, T. YAMADA, T. MATSUSHITA, H. KIYOKU, Y. SUGIMOTO, T. KOZAKI, H. UEMOTO, M. SANO, K. CHOCHO, Appl. Phys. Lett., 1998, **72**, 211.
35. A. USUI, H. SUNAKAWA, A. SAKAI, A. YAMAGUCHI, Jpn. J. Appl. Phys., 1997, **36,** L899.
36. O. H. NAM, M. D. BREMSER, T. ZHELEVA, R. DAVIS, Appl. Phys. Lett., 1997, **71**, 2638.
37. K. KUMAKURA, T. MAKIMOTO, N. KOBAYASHI, Jpn. J. Appl. Phys., 2000, **39**, 2428.
38. P. KOZODOY, M. HANSEN, S. P. DENBAARS, U. K. MISHRA, J. KAUFFMAN, Appl. Phys. Lett., 1999, **74**, 3681.
39. R. C. TU, W. H. KUO, T. C. WANG, C. J. TUN, F. C. HWANG, J. Y. CHI, J. T. HSU, Proc. of the 4th Int. Symp. Blue Laser and Light Emitting Diode, Cordoba, Spain, 2002, 1.
40. R. C. TU, C. J. TUN, J. K. SHEU, W. H. KUO, T. C. WANG, C. E. TSAI, J. T. HSU, J. CHI, G. C. CHI, IEEE Electron. Dev. Lett., 2003, **24,** 206.
41. K. WATANABE, J.R. YANG, N. NAKANISHI, K. INOKE, M. SHIOJIRI, Appl. Phys. Lett., 2002, **80**, 761.
42. Z. LILIENTAL-WEBER, Y. CHEN, S. RUVIMOV, J. WASHBURN, Phys. Rev. Lett., 1997 **79,** 2835.
43. X. H. WU, C. R. ELSASS, A. ABARE, M. MACK, S. KELLER, P. M. PETROFF, S. P. DEN BAARS, J. S. SPECK, Appl. Phys. Lett., 1998, **72**, 692.
44. Y. CHEN, T. TAKEUCHI, H. AMANO, I. AKASAKI, N. YAMADA, Y. KANEKO, S.Y. WANG, Apply. Phys. Lett., 1998, **72**, 710.
45. K. WATANABE, J. R. YANG, S. Y. HUANG, K. INOKE, J. T. HSU, R. C. TU, T. YAMAZAKI, N. NAKANISHI, M. SHIOJIRI, Appl. Phys. Lett., 2003, **82**, 718.
46. N. SHARMA, P. THOMAS, D. TRICKER, C. HUMPHREYS, Appl. Phys. Lett., 2000, 77, 1274.
47. K. WATANABE, J. R. YANG, S. Y. HUANG, K. INOKE, J. T. HSU, R. C. TU, T. YAMAZAKI, N. NAKANISHI, M. SHIOIJIRI, Appl. Phys. Lett., 2003, **82**, 715.
48. H. SAIJO, J.T. HSU, R. C. TU, M. YAMADA, M. NAKAGAWA, J. R. YANG, M. SHIOJIRI, Appl. Phys. Lett., 2004, **84,** 2271.
49. M. D. BREMSER, W. G. PERRY, T. ZHELEVA, N. V. EDWARDS, Q. H. NAM, N. PARIKH□D. E. ASPNES, R. F. DAVIS, MRS Internet J. Nitride Semicond. Res., 1996, **1,** 8.
50. B. PECZ, Zs MAKKAI, M.A. DI FORTE-POISSON, F. HUET, R. E. DUNIN-BORKOWSKI, Appl. Phys. Lett., 2001,**78,** 1529.
51. H. SAIJO, M. NAKAGAWA, M. YAMADA, J.T. HSU, R. C. TU, J. R. YANG, M. SHIOJIRI, Jpn. J. Appl. Phys., 2004, **43**, 968.
52. M. ČEH, S. ŠTURM, H. SAIJO, J. T. HSU, J. R. YANG, M. SHIOJIRI, Proc. of the 8th Asia-Pacific Conf. of Electron Microscopy, Kanazawa, 2004, in print.